NDT&E International 144 (2024) 103074

Contents lists available at ScienceDirect

NDT and E International

journal homepage: www.elsevier.com/locate/ndteint

Towards an in-process ultrasonic phased array inspection method for narrow-gap welds

Ewan Nicolson *, Ehsan Mohseni, David Lines, Katherine M.M. Tant, Gareth Pierce, Charles N. MacLeod

University of Strathclyde, Royal College Building, 204 George Street, Glasgow, G1 1RX, UK

ARTICLE INFO

Keywords:
Ultrasonics
Weld inspection
Narrow-gap welding
In-process inspection
Phased array ultrasonic testing (PAUT)

ABSTRACT

The marriage of welding and Non-Destructive Testing (NDT) processes at the point of manufacture has enabled the detection and correction of defects during the welding process. This has demonstrated clear financial and production benefits by reducing weld rework and ensuring schedule certainty, however this is yet to be demonstrated for use with narrow-groove welding practises. Narrow-groove welds are notoriously difficult to inspect using traditional Phased Array Ultrasonic Testing (PAUT) techniques due to large thicknesses and the vertical nature of Lack-of-Sidewall Fusion (LOSWF) defects. This is further complicated by the presence of partially-filled weld geometries during in-process inspection, which cause geometric reflections which can mask or falsely indicate the presence of a defect. A solution to this is proposed in this work, by adapting a dual-tandem phased array imaging system for the imaging of LOSWF defects in a partial weld geometry. This considers a two array system utilising a phased array probe on each weld side, coupled with an advanced dual-aperture Full Matrix Capture (FMC) acquisition technique. Advanced multi-mode image processing algorithms such as the Total Focusing Method (TFM) and Phase Coherence Imaging (PCI), with adaptive delay law calculation, have shown high sensitivity to LOSWF defects in a mock partial weld geometry. Additionally, an adaptive Probe Centre Spacing (PCS) technique is defined for in-process inspection based on amplitude and phase coherence sensitivity in partial weld geometries, with the effects of partial weld reflections analysed and discussed. These results have demonstrated the effectiveness of a dual-tandem phased array approach to imagine LOSWF defects during the in-process inspection of narrow-gap welds.

1. Introduction

The ability to consistently manufacture high-quality welds has been the subject of research and investment for centuries. In recent years, the innovation of nuclear energy has heightened the demand for welded components which can withstand the intense heat and pressures experienced within a nuclear reactor over several decades. The integrity of these components is crucial to the safe operation of nuclear assets, with potentially catastrophic environmental and financial repercussions for component failure.

This requirement is not unique to the nuclear industry, with numerous critical components in energy generation and storage - including pressure vessels, Hydrogen & Liquified Natural Gas (LNG) tanks and wind turbine towers – requiring high-strength precision welding. With escalating pressure to cut global carbon emissions by 2050, an increase in demand for high-integrity, cost-efficient and high-throughput welding procedures - notably in nuclear and renewable energy sectors - is clear.

Particularly within nuclear asset components, thick-section steel is typically used to withstand the high stresses observed at high temperature and pressure. The consistency of traditional welding practices tend to break down at these large thicknesses, requiring an alternative joining method. One such method is narrow-gap welding, which employs near-vertical J-groove bevel angles of 1°–6°, reducing weld volume and heat input while limiting weld distortion, shrinkage, and the Heat Affected Zone (HAZ) width [1–3]. A visual comparison between traditional V-groove weld and narrow gap J-groove geometries are shown in Fig. 1. Ultimately, the narrow-gap groove allows high integrity thick-section welding to be performed time efficiently at a lower cost to the manufacturer.

Narrow-gap grooves requires the adaption of typical welding techniques, including Submerged Arc Welding (SAW), Metal Inert/Active

* Corresponding author.
E-mail address: ewan.nicolson@strath.ac.uk (E. Nicolson).

https://doi.org/10.1016/j.ndteint.2024.103074
Received 5 October 2023; Received in revised form 21 December 2023; Accepted 18 February 2024
Available online 20 February 2024

Gas (MIG/MAG) welding and Tungsten Inert Gas (TIG) welding. A steep bevel geometry coupled with large thicknesses limits access when welding, and necessitates the use of specialised equipment and highly skilled operators to ensure weld quality. This space constraint leaves narrow-gap welds more susceptible to fusion flaws, namely Lack-Of-Sidewall Fusion (LOSWF), where deposited weld material does not sufficiently fuse to the parent substrate [4]. The result is a planar crack-like defect that runs along the weld bevel. If left untreated, static and dynamic loading experienced through component lifetime can cause further fatigue cracking from the LOSWF, requiring rework or scrapping, and potentially leading to critical component failure if uncorrected. It is therefore critical that such defects are detected and corrected before use.

Non-Destructive Testing (NDT) is a process used to monitor the integrity of a welded component from manufacture to end-of-life. A weld identified as containing a defect in this process will either be monitored, repaired or scrapped – nonetheless avoiding component failure by preventing the unchecked growth of defects. With steep bevel angles and large thicknesses, relying on existing ultrasonic NDT methods for narrow-gap welds does not ensure confidence in inspection reliability. To ensure similar inspection dependability in narrow-gap welds, a dual-tandem phased array inspection method has been proposed [5]. This has been designed to maximise the performance of near-vertical flaw detection and characterisation, by deploying two phased array probes on opposite sides of the weld. This enables both reflective and diffractive flaw responses to be acquired, depending on the transmitting and receiving element considered.

The dual-tandem method has deployed advanced acquisition and image processing methods through the use of Full Matrix Capture (FMC) and the Multi-Mode Total Focusing Method (MM-TFM) [6,7]. The FMC-TFM imaging method allows uniform full aperture focusing in both transmission and reception by applying delay laws to time-trace data in post-processing, and has come to be considered the ‘gold standard’ post-processing algorithm [8]. The application of this method has been shown to increase defect detection and characterisation reliability [9–11]. However, with a recent surge in research of amplitude-free imaging, techniques such as Phase Coherence Imaging (PCI) have begun to be implemented in commercial phased array devices. PCI has been shown to reduce issues commonly experienced when relying on amplitude-dependent methods, by considering only the phase coherence of received signals [12–14]. Additionally, increased sensitivity to diffractive effects has been observed, particularly for crack-like defects [15].

An advanced path finding algorithm is also used to compute the post-processing delay laws required for the uniform focusing of algorithms such as TFM and PCI with the dual-tandem method. The Multi-Stencils Fast Marching Method (MSFMM) allows the computation of travel times through non-homogenous and anisotropic materials, with low error and efficient output. The combination of the TFM algorithm with the MSFMM path finding method has often been termed ‘TFM+’ in previous publications [16,17].

Standard welding procedures [18,19] dictate that the NDT process should occur after the welding process is complete - given sufficient time for cooling defects to form. However, defects detected after manufacture, particularly in multi-pass welds, can require extensive rework to excavate the weldment and repair the defective area. Delays for rework risk schedule certainty and increasing production costs, which can cause knock-on production delays. This can be avoided with continuous in-process weld inspection during deposition, allowing flaws to be detected as they form. Defective areas can then be reworked between weld passes without extensive excavation, and with minimal process disruption. Schubert et al. have demonstrated the ability to detect flaws using an in-process laser welding inspection using several methods, including acoustic emission, laser speckle photometry and Phased Array Ultrasonic Testing (PAUT) [20,21]. The design of an inline PAUT system consisting of high-temperature wedges and cooling system is shown for narrow grooves, and confirms the validity of pursuing a purely ultrasonic in-process inspection method for narrow-gap fusion welding.

The use of liquid-filled high-temperature dry-coupled ultrasonic wheel probes have shown high performance in-process inspection of both V-groove welds and Wire + Arc Additive Manufacturing (WAAM) using traditional PAUT methods [22–24]. These wheel probes have demonstrated tolerance to process temperatures of up to 350 °C experienced due to close proximity to the welding process. As a typical immersion array can withstand temperatures up to 60 °C, thermally insulating materials and tight thermal management are vital to ensure reasonable operating conditions within the wheel probe. This has allowed continuous inspection of components during manufacture, as well as monitoring of hydrogen cracking post-weld for up to 96 h [25]. In addition, this has been combined with a robotic welding infrastructure to provide a combined automated in-process inspection and welding technique [26], ensuring the consistency of both processes. Ultrasonic data obtained in-process has also been used for real-time monitoring and adjustment of welding processes to actively prevent defects forming [27]. The ability to transmit ultrasound with a dry-coupling technique allows safe use during the welding process without contamination of the weld through liquid-coupling. However, this has not yet been demonstrated for narrow-groove weld geometries.

Thus far, the effectiveness of the dual-tandem phased array method has been demonstrated in mock narrow-groove samples containing near-vertical notches to simulate LOWSF defects - considered a ‘cold’ inspection of a completed weld. This work will begin to explore the application of the dual-tandem method as an in-process narrow-gap weld inspection technique. In theory, an in-process technique would provide significant time and cost benefits to narrow-gap welding, as large thicknesses and steep bevels not only complicate the welding and inspection processes, but also the rework process. A potential flaw detected in a cold-scanned component may require the removal of several deposited passes for correction. This can be challenging and time inefficient, with negative knock-on effects on production throughput, as well as risking component integrity due to significant grinding.

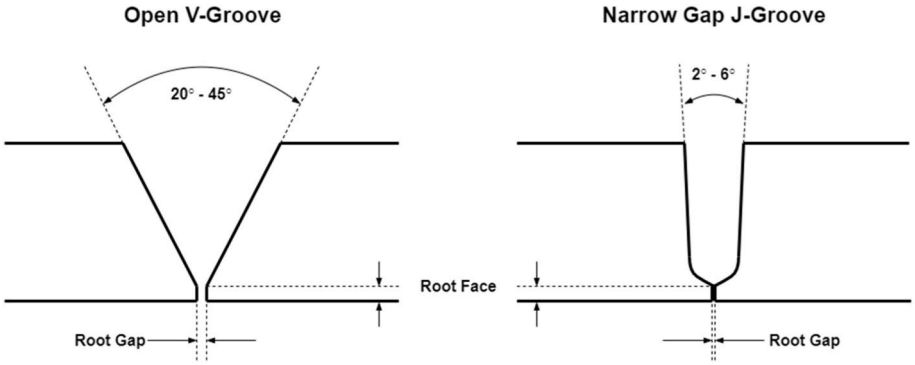

Fig. 1. Traditional V-groove (left) and narrow gap J-groove (right) bevel geometries.

However, contrary to the controlled environment preferred for post-manufacture component inspection, an ultrasonic in-process inspection method must maintain detection performance in adverse conditions. Partially-filled weld geometries can introduce non-defect reflections from the un-filled weld groove and uppermost pass weld cap, as well as requiring careful consideration of inspection setup at each weld pass. High temperature gradients can skew and shift ultrasound such that imaging is not properly focussed unless compensated for. Other factors such as process interference, data transfer speeds and image processing optimisation also present added challenges. These problems complicate an inspection both mechanically and ultrasonically - complicating and limiting deployment if not addressed correctly.

Key research has already been conducted to understand and address some of these issues faced during an in-process weld inspection. PAUT inspection of partial-weld geometries has shown high-sensitivity of intentionally imbedded tungsten defects in V-groove welds [28]. Thermal compensation methods have been explored using advanced ultrasonic imaging methods, shown to improve defect localisation during high-temperature inspection [29]. In the interest of reducing acquisition, transfer and processing times for real-time imaging, data reduction techniques such as single-bit PCI [30] and Plane-Wave Imaging (PWI) [31,32] acquisition have been considered in the wider literature.

By considering the application of the dual-tandem method to an in-process geometry inspection, the performance of uniform focusing methods for imaging such as PCI and TFM can be evaluated. The changing geometry observed in an in-process narrow gap inspection scenario must be considered carefully, as geometric reflections can potentially mask or present themselves as defects. A method which can ensure geometric responses do not interfere with defect detection is paramount for any in-process weld inspection technique. This work will look to consider and demonstrate the effectiveness of the dual-tandem method for in-process narrow-gap weld inspection, by considering the effect of partial weld geometries with steep bevels on mock LOSWF defects.

This paper will firstly introduce the dual-tandem method, and the process for acquiring and processing data with two phased array probes. The design and purpose of each test piece is introduced, followed by a study to optimise Probe Centre Spacing (PCS) based upon weld depth. Finally, results are presented and discussed, with plans for future work introduced.

2. Inspection method

The dual-tandem phased array method has been shown to increase sensitivity and effectiveness of near vertical defects in mock narrow-gap weld inspection [5]. By utilising a dual-array setup across the weld, a symmetrically uniform sensitivity of reflective phenomena at each weld side is achieved. Particularly when considering in-process inspection, this reduces the need to conduct two individual scans on both weld sides. Furthermore, the ability to perform through-weld propagation can increase the sensitivity of the system to diffractive effects, allowing tip diffraction indications to be detected and accurate flaw sizing.

Imaging using the dual-tandem method has been performed by using post-processing algorithms such as TFM on FMC acquisition data. The remainder of this section will briefly outline the software and hardware requirements of this method, as well as the acquisition and image processing algorithms used.

2.1. Hardware & software

The hardware used in this work required for the dual-tandem phased array method is outlined below. Two arrays with Rexolite wedges were used in conjunction with a PEAK-NDT phased array controller. The angle of these wedges were determined by analysis of longitudinal and shear transmission angles, and chosen to ensure suitable transmission of wave modes [5]. A photo of the dual-tandem setup using this hardware is shown in Fig. 2.

- 2x: 5 MHz, 64-element Olympus A32 phased array probes (*0.5 mm pitch*)
- 2x: 60LW Olympus A32 Rexolite wedge (*20° wedge angle,* 2330ms^{-1} *velocity*)
- PEAK-NDT MicroPulse 6 phased array controller (*128/256 channel*)

All data was collated and saved using a LabView [33] acquisition programme which interfaces with the PEAK-NDT array controller. FMC data was then saved in Multi-Frame Matrix Capture (MFMC) [34] file format. Post-processing was conducted offline in a MATLAB-based programme [35], with GPU accelerated imaging code created using MathWorks GPU Coder software [36], and path-finding algorithms accelerated with MathWorks Parallel Computing toolbox [37].

2.2. Full Matrix Capture

Traditionally, FMC acquisition occurs across the full aperture of a single array, where responses are recorded from each element for the iterative transmission across each individual element. However, the dual-tandem method expands this method over two array apertures. This can be simplified by assuming both arrays each contribute to half of a greater single aperture, and performing a 'Dual Aperture' FMC (DAFMC) acquisition. The resulting dataset can be separated into four unique subsets, each containing data pertaining to a different system 'view' - relating to two pulse-echo and two through-weld transmission subsets.

As this can be performed in a single acquisition sequence, without the requirement for multiple firings, the acquisition time relative to a single array is doubled. Using techniques such as TFM and PCI, a single DAFMC dataset can be used to generate an image for each of the four views for a given wave mode.

2.3. Time of flight calculation

With the added complexity of the partial weld geometry, careful consideration is required when approaching Time-of-Flight (ToF) calculations required for the uniform focusing involved in post-processing imaging algorithms. To ensure ToF values that accurately represent the propagation of waves throughout the image domain, it is important that the weld geometry at a given pass is known, such that it can be considered in calculations. The accuracy to which this geometry is known will directly influence the quality of the image produced. However, during the welding process, the exact geometry of the weld cap cannot precisely be known without increasing the complexity and time of the inspection process – counter to the benefit of in-process inspection. From a Weld Procedure Specification (WPS), a pre-emptive

Fig. 2. Dual-tandem setup with two opposite-facing 5 MHz 64-element arrays mounted on 60LW Rexolite wedges.

approximation of the cap geometry can be made for each weld pass, and used to compensate the ToF values calculated for a given pass.

Numerous methods have been demonstrated for the calculation of ToF values used in post-processing algorithms. These include iterative bisection methods for multiple layers of homogenous and isotropic materials [38,39], as well as the A* [40] and Dijkstra [41] path finding algorithms for anisotropic materials.

The Multi-Stencils Fast Marching Method (MSFMM) [42] is an adaption of the Fast Marching Method (FMM) [43]. A path finding forward model the MSFMM computationally solves both the non-linear Eikonal equation and wider static Hamilton-Jacobi equations, and has shown to reduce errors relative to traditional FMM methods [44]. Given a known transmitter $t_{x,y}$ within a discretised velocity field $V(x,y)$ describing the domain $I(x,y)$, the minimum travel time $\Delta\tau$ to the point $(x_i,y_i) \in I$ can be found using an upwind finite difference scheme shown in *Eq. (1)*.

$$\left|\Delta\tau\left(x_i,y_i,t_{x,y}\right)\right| = \frac{1}{V(x_i,y_i)} \qquad \text{Eq. (1)}$$

The MSFMM can be and has been used with ultrasonic NDT methods for the calculation of travel-times in both isotropic [5,16,29] and anisotropic [17,45] materials.

Due to the efficiency of the MSFMM, and the ability to compute multiple elements in parallel, its use for the calculation of ToF maps for use with advanced ultrasonic phased array techniques is clear. Furthermore, as only the velocity field $V(x,y)$ and source positions $t_{x,y}$ are required, the MSFMM can be easily adapted to consider applications with velocity variations due to temperature, and partial weld geometries.

In reality, the cap of a recently deposited weld pass is not uniform or flat, due to the weaving nature of the welding process. The geometry of this cap can be difficult to accurately predict, and therefore is difficult to compensate for in delay law calculations. Therefore, in this work a perfectly flat weld cap will be used, considering only the bevel geometry and filled weld height.

Fig. 3 shows an uncompensated and compensated pulse-echo ToF map, for a 30 mm filled partial weld geometry in a 120 mm plate. It is clear that there are significant shifts in the ToF on the far weld side when compensating for the weld, as waves are prevented from crossing the air gap in the unfilled weld portion.

2.4. Total Focusing Method

The TFM algorithm allows post-processing of a full matrix dataset, as proposed by Holmes et al. in 2005 [46], and in accordance with international testing standard [47]. The algorithm performs pseudo-focusing of a full array aperture in both transmission and reception at every point in a discretised image domain. This requires extensive delay law generation, which is efficiently generated by a ToF map for a given pair of transmitting τ_{tx} and receiving τ_{rx} elements. Values in the ToF map can be used to apply post-processing delay laws across an aperture for focusing at each discrete point in an image domain.

Considering the dual-tandem setup, with DAFMC acquisition, a TFM image of a given view can be calculated using Eq. (2). The Hilbert transform $\hat{u}(t)$ of the dataset allows the computation of a point (x_i,z_j) in an analytic image, by calculating the envelope of individual A-Scans. The pixel amplitude of a resulting image is the sum of amplitude values across each of the N^2 transmit-receive element pairs. The element

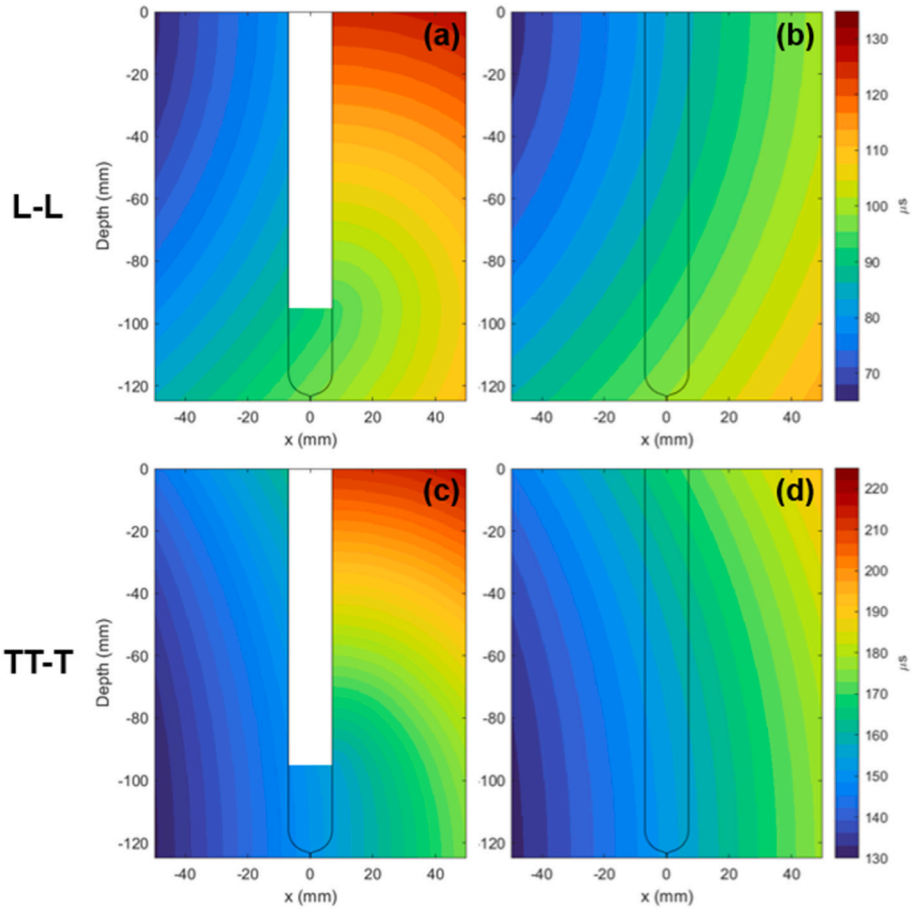

Fig. 3. Example of ToF compensation for a partial weld geometry, for pulse-echo L-L mode (a) compensated and (b) uncompensated for geometry, and for pulse-echo TT-T mode (c) compensated and (d) uncompensated for weld geometry.

indices used in transmission N_{tx} and reception N_{rx} are dependant on the 'view' required to be imaged by the dual-tandem system, and relate to the relevant elements used in the desired subset of the DAFMC data.

$$I_{TFM}(x_i, z_j) = \frac{1}{N} \sum_{tx=1}^{N_{tx}} \sum_{rx=1}^{N_{rx}} \hat{u}_{tx,rx}\left(\tau_{tx}(x_i, z_j) + \tau_{rx}(x_i, z_j)\right) \quad \text{Eq. (2)}$$

TFM has several advantages over traditional PAUT techniques, with the main benefit being the uniform focusing power. Additionally, improved spatial resolution, geometric and wave speed correction ability, and reduced dead zones give TFM an advantage over PAUT. However, unknown component geometries, large data files and lack of available operator training still negate the use of TFM for some applications.

2.5. Phase Coherence Imaging

Phase Coherence Imaging (PCI) is an amplitude-free alternative algorithm to TFM. Contrary to TFM, an image is constructed based upon the coherence of reflector phase across A-Scans in an FMC dataset. There have been several NDT methods proposed for the computation of a phase-based image. Initially, phase-weighted TFM imaging was introduced with the Sign Coherence Factor (SCF) and Phase Coherence Factor (PCF) by Camacho et al. [12], followed by the Vector Coherence Factor (VCF) by Cruza et al. [14]. Despite no official standard currently existing, purely phase driven imaging has grown in prominence - particularly for crack-detection and monitoring [13,15].

PCI has begun to be incorporated in commercial phased array systems, despite the absence of defined standard inspection procedures. Despite this, PCI has the potential to gain a significant advantage over amplitude-based phased array methods, due to the minimal calibration procedures required. Most calibration processes for PAUT and TFM are required to ensure a uniform sensitivity over time using Time Varying Gain (TVG), and to ensure image normalisation against a reference flaw amplitude or analytical model. With PCI, flaw amplitude is not important, given that a reflector's signal amplitude is distinguishable from noise. Therefore, no calibration is required, with normalisation against a maximum phase coherence value of M – the number of A-scans used to create the image.

The amplitude free nature of PCI reduces the effect of attenuation on imaging performance, and has been shown to increase sensitivity to diffractive effects, relative to amplitude-based algorithms [13]. This improves flaw sizing, where amplitude drop methods can provide unreliable results. PCI calculation has also been shown to allow reduced data transfer and processing times, due to the ability to binarize data using a single bit sample method [30].

An example of the amplitude and phase of simulated A-Scans containing Gaussian pulses with added random noise is shown in Fig. 4(a) and (b) respectively. The phase coherence of the pulses is clear to see on the right of the figure, with the random noise exhibiting no coherence across the A-Scans. Over large A-Scan datasets such as FMC, the phase contributions of the random noise will sum to zero, whereas the coherent pulse phase will sum to a maximum. This is the principle of PCI.

Fig. 4(c) shows that phase coherence is conserved when considering only the sign of the A-Scan, rather than the full phase value. In this work, a sign-based PCI algorithm is used. This reduces required computation by eliminating the need to calculate the phase value, and increases the algorithm speed with negligible compromise in image quality.

The PCI algorithm considers the sign of a sample in the FMC dataset $\hat{u}_{tx,rx}(t)$, which is replaced by a binary value $s_{tx,rx}(t)$ (see *Eq. (3)*). *Eq. (4)*

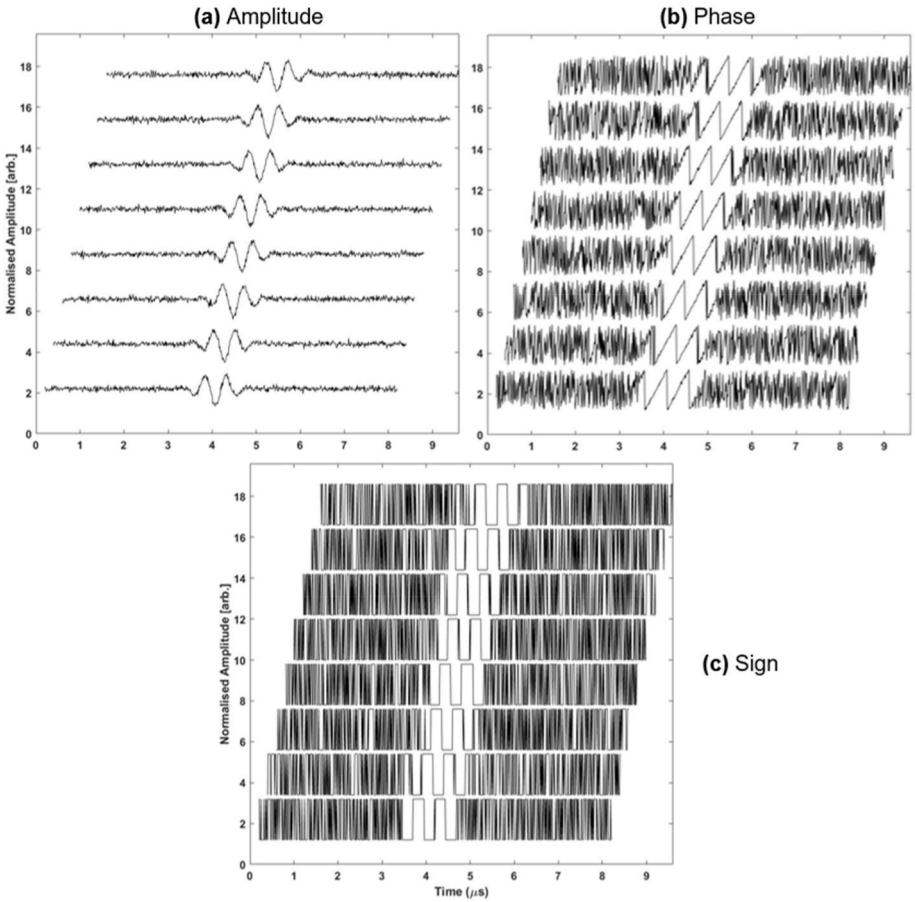

Fig. 4. (a) Amplitude, (b) phase and (c) sign of simulated Gaussian pulse A-Scans.

demonstrates that the resulting image is processed similarly to TFM, where each pixel's value is the sum of the binary coherence values of each transmit-receive element pair. Signals from reflectors will demonstrate phase coherence at a given pixel (x_i,z_j), and approach a full coherence value of M or -M, while randomly distributed noise will be incoherent across the dataset and approach zero.

$$s_{tx,rx}(t) = \begin{cases} 1, if\ \widehat{u}_{tx,rx}(t) \geq 0 \\ -1, if\ \widehat{u}_{tx,rx}(t) < 0 \end{cases} \quad \text{Eq. (3)}$$

$$I_{PCI}(x_i,z_j) = \left| \frac{1}{M} \sum_{tx=1}^{N_{tx}} \sum_{rx=1}^{N_{rx}} s_{tx,rx}\left(\tau_{tx}(x_i,z_j) + \tau_{rx}(x_i,z_j)\right) \right| \quad \text{Eq. (4)}$$

The PCI benefits from large element numbers, such that the resolution of coherence between coherent and incoherent signals is increased, which can be exploited using the dual-tandem method. Furthermore, heightened sensitivity to diffractive effects can benefit the detection of LOSWF defects in both pulse-echo and through-transmission views.

2.6. Data fusion

There are many ways in which the approach to displaying the images generated using this method can be taken. Given the large quantity of data generated from the DAFMC, and the number of modes available to the imaging algorithm, there are numerous images available for construction. To minimise and simplify the large dataset obtained from this inspection method, the mixing of different images is necessary to supply a succinct representation of the weld integrity.

Data fusion in the form of image mixing can be approached from a number of directions depending on application, including machine learning [10,48] and linear filtering [9,49]. However, in this work, data is fused based upon the information assumed to be gained from each image.

The use of imaging with multiple sound paths has been shown to aid characterisation of defects [7]. This can be used to consider ray paths which skip from the backwall and are mode converted between shear (T) and longitudinal (L) wave modes. Direct imaging modes (L-L, T-T) are considered to be diffraction-dependant, such that little to no reflective response from defects will be seen. This is due to the acute angle of incidence of the direct ray path, as reflected energy is often directional and reflected away from the receiving array, whereas diffraction is omnidirectional. Conversely, self-tandem imaging modes (LLL, TLT) are likely to produce reflective responses due to favourable ray paths and the higher amplitude seen relative to diffraction effects.

Diffractive effects are likely to be consistently visible across each view of the dual-tandem imaging system. For this reason, the two pulse-echo images and two through-transmission images obtained from direct modes are multiplied on a pixel-by-pixel basis, to form a product image I_D for that mode.

Reflective effects are often inconsistent across each view, given the two-dimensional nature of defects in the image plane. Furthermore, through-transmission images often exhibit little to no useful defect response. In this case, the two pulse-echo images for reflective modes are summed on a pixel-by-pixel basis to form a summed image I_R for that mode.

Selected diffractive and reflective images are then normalised individually, and summed together to create a final multi-mode mixed image I_T, given by the expression in Eq. (5).

$$I_T = \widehat{I_D} + \widehat{I_R} \quad \text{Eq. (5)}$$

Given the non-linear fusion of reflective and diffractive data, it is not possible to provide a sensible SNR value for fused images. Therefore, fused images will be presented without quantitative SNR analysis. Further discussion on this image fusion process can be found in earlier work introducing the dual-tandem method [5].

The mixed image will be presented with different normalisation for TFM and PCI. The TFM mixed image is normalised to either the maximum pixel value in the image, or a common normalisation value for comparison of multiple images.

For mixed PCI images, normalisation is set to the maximum coherence value. This value is the number of A-Scans used for a single image reconstruction, which in this case for a single PCI image using two 64-element arrays is $N = 16,384$. The maximum coherence for a mixed image is therefore given by Eq. (6), where M_D and M_R are the number of diffraction and reflection modes used in the mixed image respectively. As the diffraction mixing considers all four views of the image, the number of images used is $4M_D$, similarly the number of reflection images is $2M_R$ as only the two pulse-echo views are considered.

$$N_{mix} = N^{4M_D} + 2M_R N \quad \text{Eq. (6)}$$

As a value of maximum coherence in a mixed image would require a pixel to exhibit maximum coherence across all images used, the resulting normalised mixed PCI image often exhibits low coherence, even if the coherence of individual images remains high. For this reason, mixed PCI images are presented on a reduced coherence colour scale in the range of 0%–25% of the maximum coherence.

3. Partial weld samples

In order to test the dual-tandem method for in-process narrow-gap weld inspection, mock narrow-gap geometries were created to replicate a partially-filled narrow groove. The samples themselves are 125.0 mm thick A36 mild carbon steel blocks, 500.0 mm in length and with a width of 30.0 mm.

These were created to simulate a partial weld geometry at three stages of the welding process; with filled 'weld' heights of 104.0 mm, 70.0 mm and 37.5 mm. Fig. 5 shows the geometry of the three weld heights. The weld geometry attempted to mimic a 4° inclusive narrow-gap weld, with 2.0 mm root height and 5.0 mm radius.

To simulate the existence of a LOSWF defects in these samples, notches created using Electrical Discharge Machining (EDM) were machined into the steel blocks. These were 5.0 mm in height and 1.0 mm wide, rotated at 2° to match the bevel angle, and machined 10.0 mm into the 30.0 mm block thickness. These were positioned approximately 5.0 mm below the partially filled weld cap on one side – the geometry of the three samples with EDM notches are pictured in Fig. 6.

The samples will be referred to as Partial Narrow Gap (PNG) for the remainder of this work, with definitions outlined in Table 1. Six total samples were created, two for each weld fill height defined above. This consists of one defective sample containing an EDM notch, and a 'clean' sample for comparison purposes.

It should be noted that effects observed in real in-process weld inspection cannot be modelled using these samples. One such effect is high temperature gradients, which can skew ultrasonic waves and cause defect positional errors. Additionally, microstructure effects seen by a Heat Affected Zone (HAZ) are not modelled. These samples aim to simulate the effects of a partial weld in ideal conditions, at a steady room temperature and with no HAZ effects.

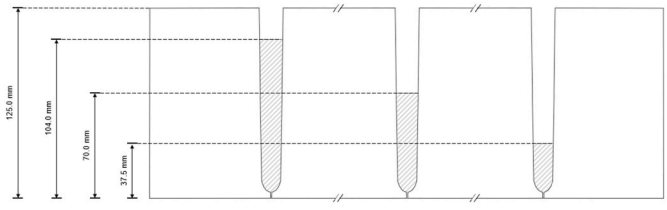

Fig. 5. Partially filled weld samples with weld fill of 104.0 mm, 70.0 mm and 37.5 mm.

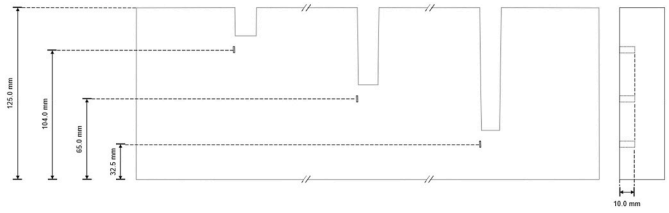

Fig. 6. EDM notch position and through-thickness depth in mock partial narrow-gap samples.

Table 1
Sample labels and geometry.

Label	Weld Fill Hight (mm)	Notch Height (mm)
PNG1	*104.0*	-
PNG2	*104.0*	*97.5*
PNG3	*70.0*	-
PNG4	*70.0*	*65.0*
PNG5	*37.5*	-
PNG6	*37.5*	*32.5*

4. Adaptive PCS

The separation of the two ultrasonic phased array probes is described by the PCS. This defines the separation between the centre element (element $N/2$) of two opposing N-element arrays, as demonstrated in Fig. 7.

To maximise full weld thickness coverage, a 'full thickness' PCS where the longitudinal crossover of the two arrays is at a depth equal to 2/3 of the sample thickness is preferred [5], similar to standard inspection procedure for Time of Flight Diffraction (TOFD) techniques [50]. However, when considering an in-process inspection scenario with partial weld geometries, full thickness coverage is not necessarily be desirable, as each pass can be inspected individually as deposited. Consequently, an adaptive inter-pass PCS can be employed, concentrating acoustic energy towards the current pass, with less importance given to formerly inspected and unfilled weld sections. The pre-defined full thickness PCS can then be used for a final full thickness cold inspection, required by international standard [18].

In order to ascertain a reference depth value for calculation of the PCS for a given weld pass, it is necessary to conduct a study using various calculation values. Similar to the full thickness PCS, a value can be calculated such that there is a longitudinal crossover at a given reference depth. This is based upon the filled weld portion, and will consider PCS values for longitudinal crossover points of 1/3, 1/2 and 2/3 relative to the top of the most recently deposited pass. Fig. 8 shows an example of PCS defined as 1/3 of the filled weld in sample PNG5, at 372.3 mm.

This study was conducted for the three samples containing EDM notches; PNG2, PNG4 and PNG6.

Images were generated using the direct L-L mode as the diffractive mode and TL-T and TT-T as the reflective modes for each sample. These were chosen as the most suitable modes based upon analysis of the useful notch indications across all direct and self-tandem image modes. This was done manually based upon the quality and SNR. However, as discussed in Section 2.6, there are a number of machine learning and

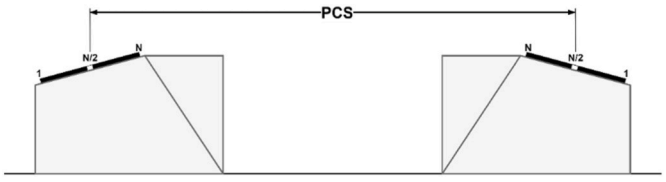

Fig. 7. PCS definition for two N-element arrays.

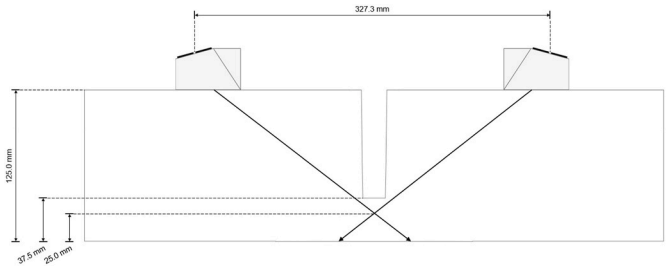

Fig. 8. 1/3 filled weld longitudinal beam crossing for PCS calculations on sample PNG5.

statistical methods which could be used to fuse multi-view images.

Fig. 9 shows the defect responses, with amplitude normalised relative to the maximum defect response, and phase to the maximum coherence value. Both the L-L and TT-T mode amplitude responses decrease with increasing PCS. This is also true for the phase coherence of the TT-T mode, however the L-L coherence exhibits the greatest response at 1/2 PCS definition. However, the TL-T mode behaves differently with changing PCS. The amplitude at 1/2 definition is greater than that of the other PCS values for both phase and amplitude – particularly amplitude. Solely, from this data, it is difficult to define an optimum PCS value for this sample, as it appears mode dependent. However, it could be argued that 2 of the three modes are optimum at the 1/3 definition, despite the TL-T mode exhibiting a far greater amplitude at the 1/2 definition.

Fig. 10 demonstrates the same trend for modes L-L and TT-T in sample PNG4, with the exception of the L-L mode response exhibiting a maximum at the 1/2 fill PCS definition. However, the TL-T trend differs greatly, and falls in line with the TT-T modes – with decreasing amplitude and phase indications with increasing PCS. This suggests that the 1/3 definition is the desirable PCS for this sample.

Fig. 11 also suggests that the 1/3 fill definition provides the best defect response for sample PNG6. Both the direct L-L mode and TT-T mode drop in amplitude with increasing PCS suggesting that the 1/3 definition is optimum. However, the phase coherence remains consistent for both modes. The TL-T phase coherence also remains fairly steady across the differing PCS, but amplitude response drops.

It should be noted that differences in a defect response amplitude can be caused by coupling variations between frame capture. To eliminate this as a potential source of error, analysis of the amplitude response from the backwall of each frame using the direct shear T-T mode was conducted, allowing the amplitude variation due to coupling to be quantified. Fig. 12 shows the backwall response amplitude, normalised to the maximum response. The coupling variation could be assumed to be a significant contributor to any differences in response between frames, given that the same excitation voltage and post-gain was used for each. It is clear that there is no significant coupling deviation across each frame from the three samples, indicated by a backwall variation of less than 3 dB across datasets. Therefore the trend in amplitude response in this PCS study is unlikely to be significantly impacted by coupling variation.

A consistent PCS definition means that a lookup table can be

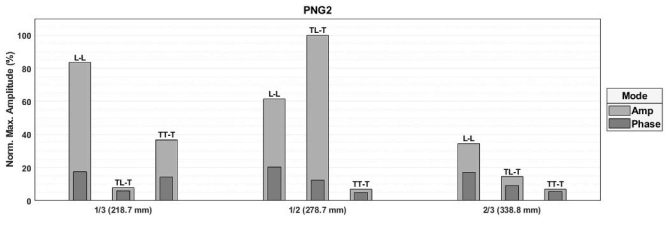

Fig. 9. Defect response amplitude and phase coherence for L-L and TL-T modes in PNG2 mixed image.

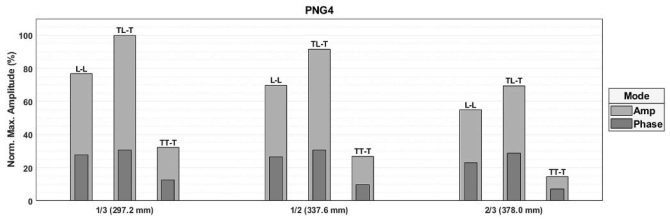

Fig. 10. Defect response amplitude and phase coherence for L-L and TT-T modes in PNG4 mixed image.

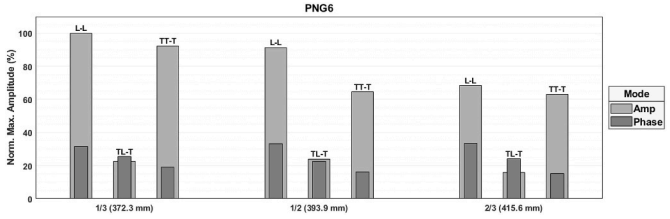

Fig. 11. Defect response amplitude and phase coherence for L-L and TT-T modes in PNG6 mixed image.

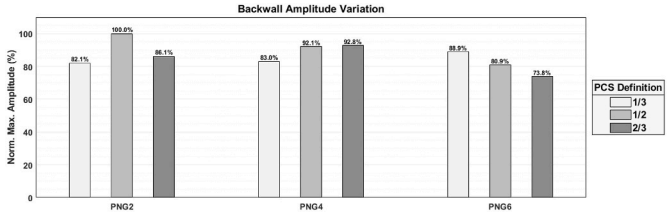

Fig. 12. Coupling variation analysis using backwall signal of T-T mode for each PCS in each sample.

generated, defining the PCS for any given plate thickness and weld fill height, as shown in Fig. 13 (for thicknesses of 16 mm–150 mm).

This study was performed on modes selected quantitatively based on image performance. However, as further outlined in the Future Work section, the development of an algorithm to quantitatively calculate the optimum PCS and modes used at a given weld height would greatly benefit a method such as this.

5. Imaging

This section will present and analyse the TFM and PCI image performance when inspecting samples containing EDM notches (samples PNG2, PNG4 & PNG6). As described in Section 2.6, images are mixed by considering modes which contribute with either diffractive and reflective responses. Furthermore, as concluded from the previous adaptive PCS study, a PCS definition of 1/3 of the weld fill height is used. A summary of both the diffractive and reflective modes used in each mixed TFM and PCI image, as well as the PCS used for each sample, is found in

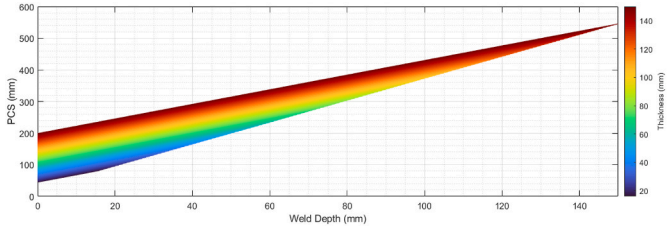

Fig. 13. 1/3 weld fill PCS definition for varying plate thicknesses and fill heights.

Table 2
Summary of mixed images from each notch sample.

Sample	Diffractive Mode	Reflective Modes	PCS (mm)
PNG2	*L-L*	*TL-T, TT-T*	*218.7*
PNG4	*L-L*	*TL-T, TT-T*	*297.2*
PNG6	*L-L*	*TL-T, TT-T*	*327.5*

Table 2.

5.1. Partial-weld imaging

Mixed TFM and PCI images for samples PNG2, PG4 and PNG6 were generated using the diffractive L-L mode and reflective TL-T and TT-T modes. The resulting images are found in Fig. 14, with images from each sample across the rows and the TFM and PCI images on the left- and right-hand columns respectively as labelled. Both TFM and PCI images are shown in a linear colour scale, with TFM normalised to each image maximum, and PCI normalised to the maximum possible phase coherence – shown on a 0%–25% scale. The PCS values used to generate each image is as defined in Table 2.

Fig. 14(a) and (b) highlight the mixed image from the shallowest notch (97.5 mm from backwall), simulating a LOSWF defect in the latter passes of the welding process. It is clear from both images that the notch can be resolved clearly. There is also little to no contribution from the weld geometry in both images.

The images of notch placed at the centre of the weld (65 mm from backwall) – around halfway through the welding process – shows similar characteristics. Fig. 14(c) and (d) both indicate the presence of the notch, however, the TFM lacks the ability to resolve the full body of the notch, and instead a top-tip diffraction indication dominates. Less clearly is the presence of the bottom tip-diffraction. Measurement of the separation of these indications presents a notch length of 5.6 mm, which is accurate to within a millimetre of the true notch size.

Additionally, significant reflections from the unfilled bevel can be seen at the top of these images. These encroach below the weld fill in the PCI image, but with a relatively low coherence value relative to the notch. Reflections in the TFM image also encroach below the weld fill, but again with an amplitude less than 50% that of the notch response.

Finally, Fig. 14(e) and (f) display images from the deepest notch (32.5 mm from backwall). Again, clear notch responses are seen in both the TFM and PCI images. Again, responses from the weld geometry are also seen, which encroach below the weld fill in both images. However, like images from the previously discussed sample, the response is low relative to that of the notch response.

It is therefore clear that using the method outlined in this work, simulated LOSWF can be clearly and accurately detected in mock partial narrow-gap samples at various points in the welding process.

5.2. Weld geometry reflections

The images presented in the previous section display minimal geometric responses, with arguably little or no impact on the resolution of the notch. However, it is important to understand the impact of geometric indications so as to avoid occurrences of defect masking or false positives. Reflective responses from the weld geometry will likely cause minimal disruption to the inspection integrity, as they appear along the unfilled bevel. The problematic response would be diffractive in nature, emanating from the corners of the partial weld cap. To understand this, diffractive responses from both the weld geometry and the notch were compared. Amplitude values were obtained using the direct longitudinal mode (L-L), as this elicited the greatest diffractive effects from both the weld geometry and notch defect.

The geometric response amplitude for the three weld heights presented in this study were obtained by inspection of samples PNG1, PNG3 and PNG5. As no notch was present in these samples, responses seen

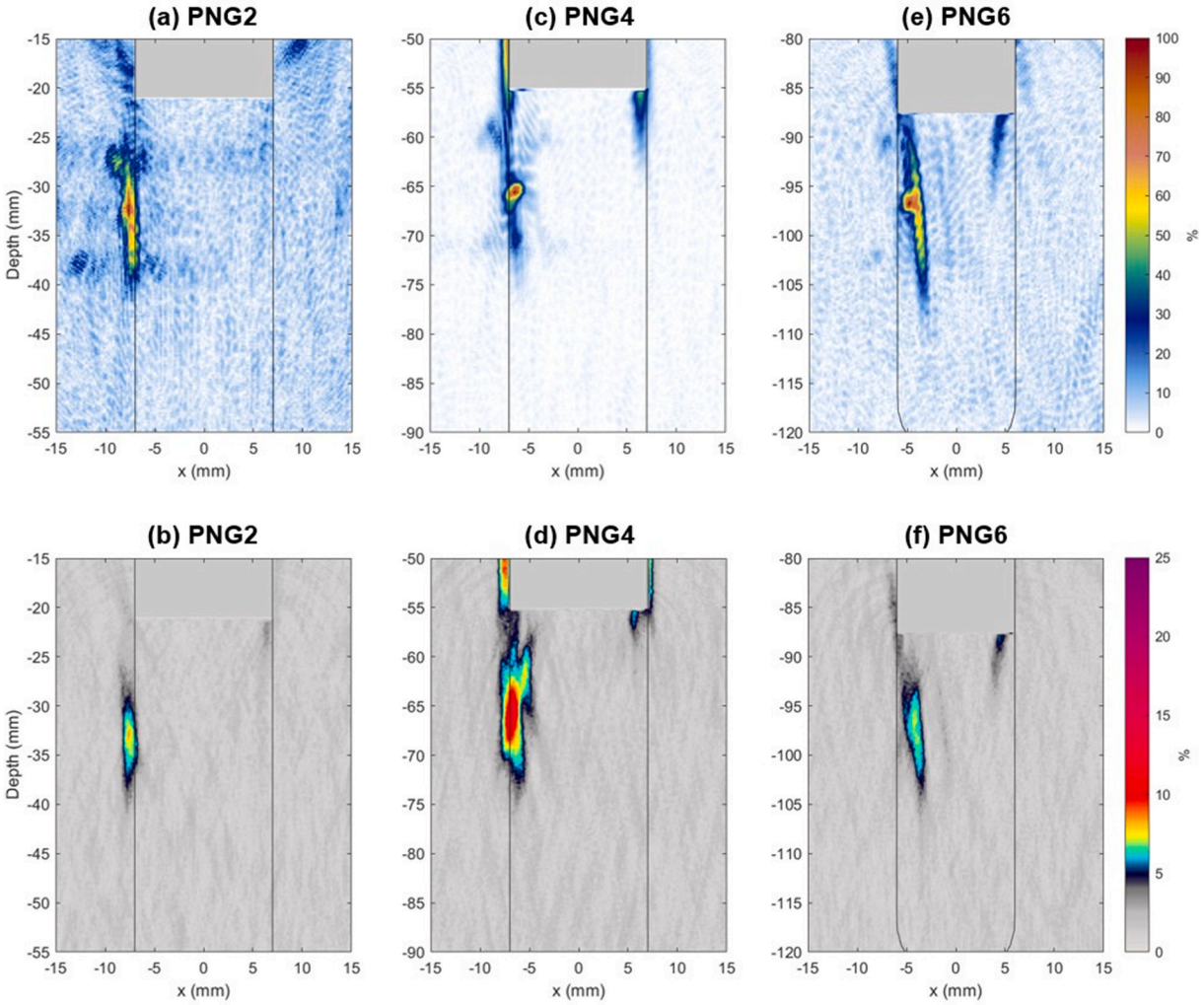

Fig. 14. Mixed TFM and PCI images of simulated LOSWF in mock partial narrow-groove samples using 1/3 weld fill PCS definition.

around the partial weld cap must be from the geometry itself. The greatest responses were observed at the corners of the partial weld cap in pulse-echo views. The amplitude of notch tip-diffraction effects were observed in samples PNG2, PNG4 and PNG6.

Fig. 15 shows the amplitude comparison, linearly normalised to the maximum observed amplitude. It is clear in each sample that the notch response is greater than the weld geometry response in each sample, with an average notch-to-weld response ratio of 6.5 dB.

It should be noted that the samples presented in this case are considered 'worst-case' in terms of weld geometry, as the unfilled weld corners are machined at a right-angles. In reality, the partial weld cap corners will not be as 'sharp', due to the behaviour of the liquid weld pool during solidification. It can therefore be hypothesised that for a real-weld geometry, the notch-to-weld response ratio will be greater.

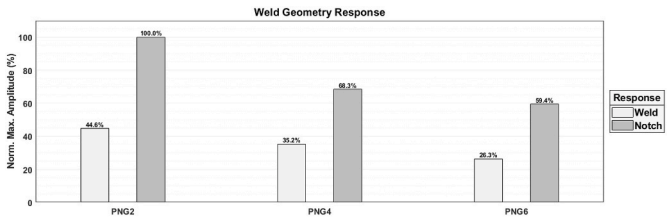

Fig. 15. Diffractive response amplitude from the weld geometry and notch tips in each mock partial narrow-gap sample.

5.3. Mode-converted diffraction

Mode-converted through-transmission imaging has been investigated for TOFD techniques for improved dead-zone imaging [51,52]. This considers direct modes with mode-conversion (either L-T or T-L). The advantage of this for TOFD is that the low-velocity of the shear leg increases the time between the lateral wave and diffracted wave – reducing dead zones typically seen with traditional TOFD.

This same method can be applied to the pitch-catch imaging of the dual-tandem method. In full-depth cold scans, this would have the same effect of reducing the lateral wave dead zone associated with TOFD [5]. However, the technique can also be applied to partial weld geometries, by increasing the time between diffracted waves and weld reflections. The main issue with this approach is the 'leaking' of other mode converted signals into the image, which can introduce the possibility of false-positive defect reports.

Fig. 16(a) shows the standard L-L pitch-catch image, showing top and bottom tip-diffraction of the EDM notch. Fig. 16(a) and (b) show the mode converted diffracted signals – L-T and T-L respectively. Although relatively lower in amplitude than the L-L mode, tip-diffraction can also be clearly seen. Additionally, geometric reflections from the partial weld also appear to be reduced. However, a significant number of additional responses are present in the images, in turn creating potential dead zones. This may not be an issue when considering in-process inspection, given that the dead zone does not interfere with the current pass being inspected.

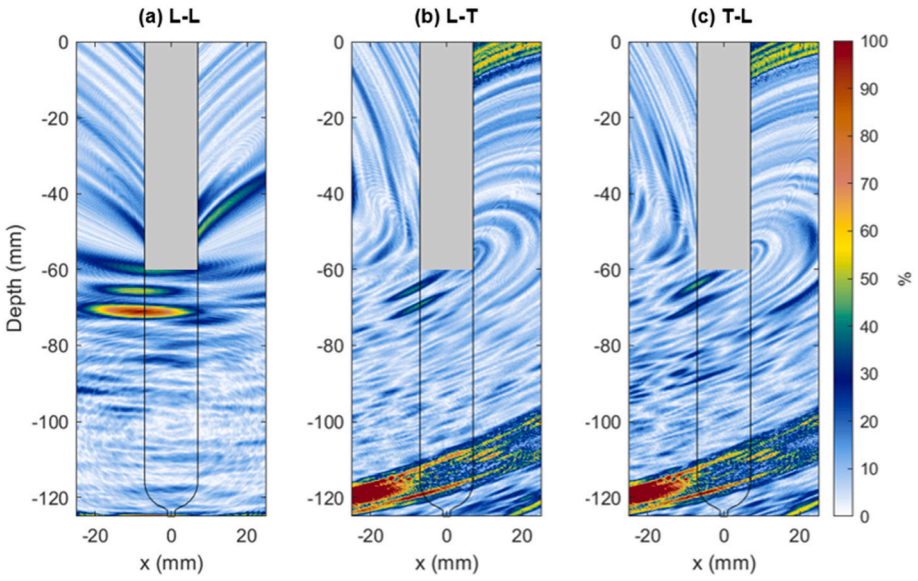

Fig. 16. Pitch-catch TFM images for sample PNG4 using mode (a) L-L, (b) L-T and (c) T-L.

The possible advantage of using mode-converted waves for pitch-catch imaging is therefore clear, and would merit consideration for future work in this field.

6. Future work

The next step to in-process narrow-gap weld inspection is the optimisation and acceleration of both hardware and software, towards a real-time inspection method. This can be achieved by implementing several methods. One such method is the development of a weld-pass dependent qualitative wave mode selection algorithm. The current qualitative technique is not suitable for an inspection process due to both speed and the possibility of human error. A sensitivity-based approach would allow pre-calculation of contributing modes for each weld pass based on a sensitivity factor, and would reduce unnecessary computation of low-contribution modes, while also limiting as much as possible any quantitative judgement required. Additionally, reflections from the partial weld cap could also be considered pre-inspection such that geometrical reflections are minimised through mode and PCS choice.

As stated in Section 5.2, the work presented here highlights the 'worst-case' partial weld geometry, where sharp corners increase diffraction responses. Application of this method to real-weld geometries would allow analysis of this method for real weld geometries, where solidification of the weld pool would soften geometrical edges in the partial geometry, potentially increasing the notch to weld geometry amplitude ratio.

To prevent damage to the phased array probe in close proximity to the high-temperature weld environment, the use of a high-temperature roller probe should be used. This would introduce added attenuation from the both the tyre and dry-coupling. The presence of temperature gradients through the roller probe will also likely effect imaging performance, with active compensation and probe cooling required.

Furthermore, robotic automation of the dual-tandem setup would be required to ensure both consistent and encoded scanning. This would necessitate accurate synchronisation of two separate robotic manipulators to ensure probes remain parallel so to ensure through-transmission imaging remains consistent across the scan.

The use of PWI can reduce both the acquisition and image processing, by reducing the amount of data collected. Additionally, the firing of multiple elements can reduce the effects of attenuation seen through the roller probe tyre. Coupled with PCI, the ability for single-bit GPU processing would greatly increase the available frame rate.

7. Conclusion

The ability to detect and correct defects during the welding process suggests obvious benefits to manufacturing costs and efficiency, particularly for thick-section welding techniques such as narrow-gap. However, geometrical reflections observed from partial weld geometries have the potential to mask or provide false-positive defects. In response, a dual-tandem phased array inspection method has been shown to provide good LOSWF detection sensitivity for partial weld geometries.

A PCS study based on amplitude and phase coherence has provided an inspection plan to maximise inspection sensitivity as the weld is filled, with good defect detection sensitivity for weld passes across the full weld thickness. This is achieved using a dual-aperture FMC acquisition method, in addition to an adaptive path-finding delay law calculation algorithm to compensate for the partial weld geometry. This has been shown with advanced offline image processing algorithms such as TFM and PCI, coupled with multi-mode image mixing techniques, to precisely and clearly detect LOSWF type defects in a partial weld geometry.

Future work includes extending this research for use with high-temperature dry-coupled wheel probes, towards an in-process inspection technique for narrow-gap welds. Additionally, a qualitative method for pre-inspection multi-mode selection, as well as improvements to acquisition and processing times, are required for implementation of this method for in-process real-time imaging.

CRediT authorship contribution statement

Ewan Nicolson: Conceptualization, Data curation, Methodology, Software, Writing – original draft, Writing – review & editing. **Ehsan Mohseni:** Methodology, Supervision, Writing – review & editing. **David Lines:** Software, Supervision, Writing – review & editing. **Katherine M. M. Tant:** Software, Supervision. **Gareth Pierce:** Supervision. **Charles N. MacLeod:** Methodology, Supervision, Writing – review & editing.

Declaration of competing interest

The authors declare that they have no known competing financial interests or personal relationships that could have appeared to influence the work reported in this paper.

Data availability

Data will be made available on request.

Acknowledgements

This work is supported by EPSRC Centre for Doctoral Training in Future Innovation in Non-Destructive Evaluation (FIND) under EPSRC Grant No. EP/S023275/1.

References

[1] Bicknell AC, Patchett BM. Heavy section weldments with a gmaw narrow gap welding process. In: Welding Institute of C, editor. Welding for challenging environments; 1986. p. 65–74. Pergamon.
[2] Hunt JF. Narrow gap welding of pressure vessels – a manufacturer's view. In: Welding Institute of C, editor. Welding for challenging environments. Pergamon; 1986. p. 107–16.
[3] Sekimura N, Yamashita N. 20-Plant life management (PLIM) practices for boiling water nuclear reactors (BWR): Japanese experience. In: Tipping PG, editor. Understanding and mitigating ageing in nuclear power plants. Woodhead Publishing; 2010. p. 706–31.
[4] Laing B, et al. Narrow gap welding of 2' Hv-100 plate using closed Loop, adaptive-feedback, through-the-Arc tracking technology. In: Welding Institute of C, editor. Welding for challenging environments. Pergamon; 1986. p. 117–29.
[5] Nicolson E, et al. Dual-tandem phased array Method for Imaging of near-vertical Defects in narrow-gap welds. NDT E Int 2023;135:102808.
[6] Holmes C, et al. Post-Processing of the full Matrix of ultrasonic transmit–receive array Data for non-destructive evaluation. NDT E Int 2005;38(8):701–11.
[7] Zhang J, et al. Defect detection using ultrasonic arrays: the multi-mode total focusing method. NDT E Int 2010;43(2):123–33.
[8] Fan C, et al. A Comparison between ultrasonic array Beamforming and super resolution imaging Algorithms for non-destructive evaluation. Ultrasonics 2014;54 (7):1842–50.
[9] Bevan RLT, et al. Data fusion of multiview ultrasonic imaging for characterization of large defects. IEEE Trans Ultrason Ferroelectrics Freq Control 2020;67(11): 2387–401.
[10] Bevan RLT, Croxford AJ. Automated detection and characterisation of defects from multiview ultrasonic imaging. NDT E Int 2022;128:102628.
[11] Budyn N, et al. Characterisation of small embedded two-dimensional defects using multi-view total focusing method imaging algorithm. NDT E Int 2021;119:102413.
[12] Camacho J, et al. Phase coherence imaging. IEEE Trans Ultrason Ferroelectrics Freq Control 2009;56(5):958–74.
[13] Camacho J, et al. Ultrasonic crack evaluation by phase coherence processing and Tfm and its application to online monitoring in fatigue tests. NDT E Int 2018;93: 164–74.
[14] Cruza JF, et al. Plane-wave phase-coherence Imaging for Nde. NDT E Int 2017;87: 31–7.
[15] Gauthier B, et al. Towards an alternative to time of Flight diffraction using Instantaneous phase coherence imaging for characterization of crack-like defects. Sensors 2021;21(3):730.
[16] Tant KMM, et al. A transdimensional bayesian Approach to ultrasonic travel-time Tomography for non-destructive testing. Inverse Probl 2018;34(9):95002.
[17] Tant KMM, et al. Effective grain orientation mapping of complex and locally anisotropic media for improved imaging in ultrasonic non-destructive testing. Inverse Problems in Science and Engineering 2020;28(12):1694–718.
[18] The British Standards Limited. Bs En Iso 17640:2018: non-destructive testing of welds – ultrasonic testing. In: Techniques, testing levels, and assessment; 2018.
[19] The British Standards Limited. Bs En Iso 19285:2017: non-destructive testing of welds – ultrasonic testing. In: Phased array ultrasonic testing (PAUT) - Acceptance levels; 2017.
[20] Schubert F, et al. Nondestructive testing and inline monitoring of laser beam narrow-gap weldings of thick metal sheets. In: 12th European Conference on non-destructive testing; 2018. Gothenburg.
[21] Schubert F, et al. Non-destructive weld inspection during the welding process - possibilities and limitations of an inline monitoring approach. In: International congresson ultrasonics. Bruges: ASA; 2019.
[22] Vithanage RKW, et al. A phased array ultrasound roller Probe for Automated in-Process/Interpass Inspection of multipass welds. IEEE Trans Ind Electron 2021;68 (12):12781–90.
[23] Mohseni E, et al. Model-assisted ultrasonic calibration using intentionally embedded Defects for in-process weld inspection. Mater Des 2021;198:109330.
[24] Vithanage RKW, et al. Development of a phased array ultrasound roller probe for inspection of Wire + Arc Additive manufactured components. J Manuf Process 2022;80:765–74.
[25] Javadi Y, et al. High-Temperature in-Process inspection Followed by 96-H robotic Inspection of intentionally manufactured hydrogen Crack in multi-pass robotic welding. Int J Pres Ves Pip 2021;189:104288.
[26] Vasilev M, et al. Sensor-enabled multi-robot System for automated Welding and in-process ultrasonic Nde. Sensors 2021;21(15):5077.
[27] Sweeney NE, et al. In-process phased array ultrasonic weld pool monitoring. NDT E Int 2023;137:102850.
[28] Javadi Y, et al. In-process Calibration of a non-destructive testing system Used for in-process Inspection of multi-pass welding. Mater Des 2020;195:108981.
[29] Foster EA, et al. Thermal compensation of ultrasonic transmit and receive data for steel welded plates at the point of manufacture. NDT E Int 2023;137:102812.
[30] Gauthier B, et al. Lightweight and amplitude-free ultrasonic imaging using single-bit Digitization and instantaneous phase coherence. IEEE Trans Ultrason Ferroelectrics Freq Control 2022;69(5):1763–74.
[31] Le Jeune L, et al. Plane wave imaging for ultrasonic non-destructive testing: generalization to multimodal imaging. Ultrasonics 2016;64:128–38.
[32] Montaldo G, et al. Coherent plane-wave Compounding for very high frame rate Ultrasonography and transient elastography. IEEE Trans Ultrason Ferroelectrics Freq Control 2009;56(3):489–506.
[33] National Instruments. Labview V17 (64-bit). 2017.
[34] Wilcox Paul. Mfmc Format 2019;2. https://github.com/ndtatbristol/mfmc.
[35] MathWorks. Matlab 2022.
[36] MathWorks. Gpu Coder 2022.
[37] MathWorks. Parrallel computing toolbox. 2022.
[38] Mineo C, et al. Solving ultrasonic ray Tracing in Parts with multiple material Layers through root-finding methods. Ultrasonics 2022;124:106747.
[39] Mineo C, et al. Generalised bisection Method for optimum ultrasonic ray Tracing and Focusing in multi-layered structures. Ultrasonics 2021;111:106330.
[40] Nowers O, et al. Ultrasonic array Imaging through an anisotropic austenitic steel weld Using an efficient ray-tracing algorithm. NDT E Int 2016;79:98–108.
[41] Nowers O, et al. Novel ray-tracing Algorithms in Nde: Application of Dijkstra and a* Algorithms to the Inspection of an anisotropic weld. NDT E Int 2014;61:58–66.
[42] Hassouna MS, Farag AA. Multistencils Fast marching methods: a highly accurate Solution to the eikonal Equation on cartesian domains. IEEE Trans Pattern Anal Mach Intell 2007;29(9):1563–74.
[43] Sethian JA. Fast marching methods. SIAM Rev 1999;41(2):199–235.
[44] Popovici AM, Sethian JA. 3-D imaging using higher order Fast marching traveltimes. Geophysics 2002;67(2):604–9.
[45] Ludlam J, et al. Travel Times and ray Paths for Acoustic and elastic Waves in generally anisotropic media. J Comput Phys 2023;494:112500.
[46] Holmes C, et al. Advanced post-Processing for scanned ultrasonic arrays: Application to defect Detection and Classification in non-destructive evaluation. Ultrasonics 2008;48(6–7):636–42.
[47] The British Standards Limited. Bs Iso 23865:2021: non-Destructive Testing — ultrasonic Testing, in General use of full matrix capture/total focusing technique (FMC/TFM) and related technologies. 2021.
[48] Siljama O, et al. Automated flaw Detection in multi-channel phased array ultrasonic data using machine learning. J Nondestr Eval 2021;40(3).
[49] Wilcox PD, et al. Fusion of multi-view ultrasonic Data for increased detection Performance in non-destructive evaluation. Proceedings of the royal society A: mathematical. Physical and Engineering Sciences 2020;476(2243):20200086.
[50] The British Standards Limited. Bs En Iso 10863:2020: non-destructive testing — ultrasonic testing. In: Use of time-of-flight diffraction technique (TOFD); 2020.
[51] Jin SJ, et al. Quantitative Detection of shallow subsurface Defects by using mode-converted Waves in time-of-flight diffraction technique. J Nondestr Eval 2020;39 (2).
[52] Jin S-J, et al. Corrected mode-converted wave Method for detecting Defects in tofd dead zone. J Nondestr Eval 2023;42(3).